Bio-Design and Manufacturing (2024) 7:1000–1017
https://doi.org/10.1007/s42242-024-00311-4

RESEARCH ARTICLE

Electrospinning/3D printing-integrated porous scaffold guides oral tissue regeneration in beagles

Li Yuan[1] · Chen Yuan[1] · Jiawei Wei[1] · Shue Jin[1] · Yi Zuo[1] · Yubao Li[1] · Xinjie Liang[2] · Jidong Li[1]

Received: 12 January 2024 / Accepted: 9 July 2024 / Published online: 2 August 2024

Abstract

The combined use of guided tissue/bone regeneration (GTR/GBR) membranes and bone filling grafts represents a classical therapy for guiding the regeneration and functional reconstruction of oral soft and hard tissues. Nevertheless, due to its displacement and poor mechanical support, bone meal is not suitable for implantation in the case of insufficient cortical bone support and large dimensional defects. The combination of GTR/GBR membrane with a three-dimensional (3D) porous scaffold may offer a resolution for the repair and functional reconstruction of large soft and hard tissue defects. In this study, a novel integrated gradient biodegradable porous scaffold was prepared by bonding a poly(lactic-co-glycolic acid) (PLGA)/fish collagen (FC) electrospun membrane (PFC) to a 3D-printed PLGA/nano-hydroxyapatite (HA) (PHA) scaffold. The consistency of the composition (PLGA) ensured strong interfacial bonding between the upper fibrous membrane and the lower 3D scaffold. In vitro cell experiments showed that the PFC membrane (upper layer) effectively prevented the unwanted migration of L929 cells. Further in vivo investigations with an oral soft and hard tissue defect model in beagles revealed that the integrated scaffold effectively guided the regeneration of defective oral tissues. These results suggest that the designed integrated scaffold has great potential for guiding the regeneration and reconstruction of large oral soft and hard tissues.

Li Yuan and Chen Yuan have contributed equally to this work.

✉ Jidong Li
nic1979@scu.edu.cn

[1] Research Center for Nano-Biomaterials, Analytical and Testing Center, Sichuan University, Chengdu 610064, China

[2] ZXTGY (Jiangsu) Technology Co., Ltd., Suzhou 215400, China

Graphic abstract

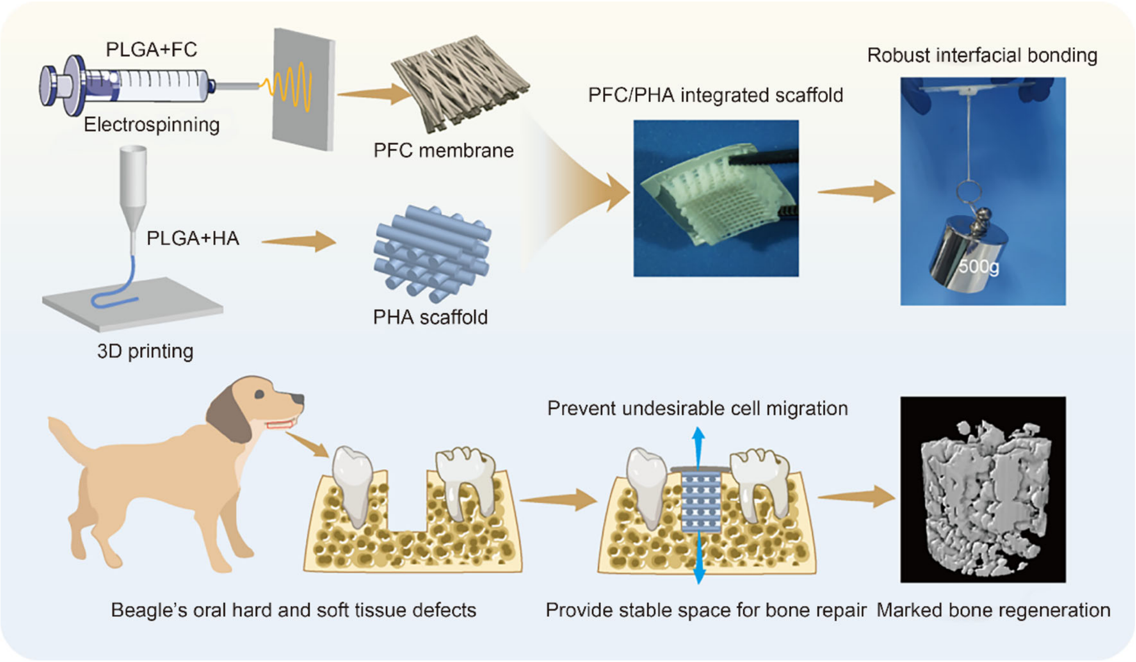

Keywords Electrospinning · 3D printing · Gradient porous scaffold · Oral tissue regeneration

Introduction

Periodontitis, one of the three major oral clinical diseases, requires tooth extraction and in severe cases, the complete removal of the infected periodontal tissue [1]. This condition leads to alveolar bone absorption, which compromises both bone volume and ridge architecture, thereby hindering the success of dental implants [2, 3]. Additionally, trauma and tumor resection can cause large alveolar and mandibular defects. The repair of oral tissue defects that exceed a critical size remains a clinical challenge and often requires the implantation of biomaterials to facilitate the repair process. Clinically, guided tissue/bone regeneration (GTR/GBR) technology is usually combined with bone grafting: the bone defect area is filled with bone grafting materials and covered with a GTR/GBR membrane to guide the regeneration and functional reconstruction of soft and hard tissues [4, 5].

Although the combined use of commercial products such as Bio-Oss bone meal and Bio-Gide collagen membrane has yielded positive clinical outcomes in guiding oral tissue regeneration, their bovine origin may pose concerns related to religious or ethnocultural issues. More importantly, the displacement tendency and poor mechanical strength of Bio-Oss bone meal hinder its application in alveolar bone defects that are large or that are associated with relatively little cortical bone support [6, 7]. Hence, there is an urgent need to develop new materials that meet the clinical requirements for regenerating large oral soft and hard tissue.

The ideal materials for guiding large soft and hard tissue regeneration should effectively prevent fast-growing fibroblasts and epithelial cells from invading periodontal defect sites, thereby creating adequate and stable space for the reconstruction of impaired periodontal tissues [8, 9]. The Bio-Gide collagen membrane is the most widely used commercially available GTR/GBR product in clinics. However, some studies have shown that the rapid degradation rate of collagen membrane prompts the loss of its space maintenance capacity under physiological conditions. Meanwhile, bovine and porcine collagen may present a risk of infection from disease (such as bovine spongiform encephalopathy and foot-and-mouth disease) and pose a problem for patients who abide by religious constraints [10–12]. Synthetic polymer-based membranes have attracted extensive interest in the field of GTR/GBR due to their simple preparation process and adjustable properties. Among the biopolymers, poly(lactic-co-glycolic acid) (PLGA) is a copolymer of polylactic acid (PLA) and polyglycolic acid (PGA), and its degradation rate can be regulated by the proportion of monomers it contains and its molecular weight [13]. Extracellular matrix-like (ECM-like) GTR/GBR membranes with good biocompatibility and mechanical properties can be obtained by co-spinning PLGA with collagen. Considering the limitations of mammalian collagen, fish collagen (FC) has recently received considerable attention in the bioengineering field due to its excellent biocompatibility, low immunogenicity, and fewer religious conflicts [14, 15]. Our previous studies have shown that the PLGA and FC composite (PFC) electrospun membranes exhibit excellent biocompatibility and promote the regeneration of both soft and hard tissues, thereby demonstrating significant application potential in GTR/GBR fields [16–18].

A single membrane or bone graft is generally unable to fulfill the requirements for regenerating large-size soft and hard tissues simultaneously. Therefore, researchers have pivoted toward developing integrated material with multiple layers by combining different types of materials in specific methods. For example, a multifunctional bi-layered "GBR scaffold" merged a loose and porous solution electrospinning (SES) writing layer with a dense and compact SES layer, using mesoporous silica nanoparticles, PLGA, and gelatin (Gel) [19]. This scaffold offered enhanced mechanical properties, a coordinated degradation profile, and a promising bone regeneration efficacy. Similarly, a novel hybrid bi-layer scaffold, which combined electrospun polycaprolactone (PCL)/Gel nanofiber membranes with three-dimensional (3D)-printed PCL/Gel/nano-hydroxyapatite (HA) scaffolds, demonstrated enhanced repair efficacy in the soft and hard tissue defects of rabbits' oral maxillary bone [20]. However, PCL-based materials degrade slowly and may persist in tissues as foreign bodies for an extended period. Therefore, it is reasonable to assume that integrating the PFC membrane with a degradation-regulated 3D-printed scaffold could potentially guide the regeneration and functional reconstruction of large soft and hard tissues in complex oral environments.

3D printing, which is a pivotal rapid prototyping technology, enables the development of complex scaffolds with precise and controllable pore structures, as well as customized shapes for the personalized treatment of bone defects. Our previous research showed that 3D-printed composite scaffolds consisting of PLGA and HA (PHA) demonstrated good osteogenic activity [21–23]. In this study, an integrated gradient porous scaffold with both excellent mechanical properties and good biocompatibility was constructed by combining PFC electrospun fibrous membrane with a PHA 3D-printed scaffold. The advantage of this design is that strong interfacial bonding between the two structural materials can be easily achieved using the same PLGA component in the upper fibrous membrane as in the lower 3D scaffold. In addition, this integrated scaffold features a relatively dense and randomly arranged nanofiber upper layer to prevent fibrous connective tissue from invading the defect area and a porous 3D scaffold lower layer to support and promote bone regeneration. After we systematically assessed the structural properties of the integrated scaffold, we set up a tissue defect model with post-tooth extraction beagles. Subsequently, the regeneration and functional reconstruction of soft and hard tissues as guided by the integrated scaffold were confirmed.

Experiments

Materials

PLGA (the molar ratio of lactic acid (LA) to glycolic acid (GA): 75:25; weight-average molecular weight (M_{w}): 90–110 kDa) was purchased from Jinan Daigang Biomaterial Co., Ltd. (Jinan, China). FC (derived from fish scale and skin) was purchased from Sangon Biotech Co., Ltd. (Shanghai, China). 1,1,1,3,3,3-Hexafluoro-2-propanol (HFIP), dichloromethane (DCM), *N*-hydroxysuccinimide, and 1-ethyl-3-(3-dimethylaminopropyl) carbodiimide hydrochloride (EDC) were obtained from Aladdin Chemical Agent Co., Ltd. (Shanghai, China). HA nanoparticles were synthesized by our laboratory according to an existing method [24]. All chemicals in the experiments were of analytical reagent grade and were used without further purification.

Preparation of PFC/PHA-integrated scaffolds

The PFC membrane was fabricated by electrospinning. FC in the amount of 0.12 g and 0.4 g of PLGA were dissolved in 2 mL of HFIP. The solutions were loaded into a plastic syringe fitted with a 21-G flat-tipped needle and fed out at a speed of 0.5 mL/h by a precision syringe pump. A high voltage of 8 kV and a tip-to-collector distance of 15 cm were used for the electrospinning. The prepared PFC membranes were placed in a vacuum oven at 25 °C to volatilize the solvent.

The PHA composite scaffold was prepared by 3D printing. In 30 mL of DCM, 5 g of HA was dispersed by vibration for 10 min, and then it was ultrasonically dispersed for another 15 min. Next, 5 g of PLGA was dissolved into the solution. The ink was loaded into a syringe equipped with a needle with an inner diameter of 0.41 mm, and was then printed by a 3D bioprinter (Regenovo, Hangzhou, China) at room temperature, with an extrusion pressure of 0.24 MPa and a printing speed of 10–15 mm/s. The thickness of each layer and the distance between each strand were set to 0.2 and 0.6 mm, respectively. The prepared scaffolds were dried in a vacuum oven until the solvent was completely volatilized.

To prepare an integrated PFC/PHA gradient porous scaffold, a small amount of DCM was smeared at the bottom of the PHA scaffold, and then promptly pressed onto the PFC fibrous membrane. The coverage area of the barrier membrane (PFC) must extend 2–3 mm beyond the edge of the bone scaffold (PHA), thereby forming a complete barrier and enabling functional osteoconductivity to facilitate the new bone formation and to reduce infection.

Structure and characterization of physicochemical properties

Scanning electron microscopy (SEM; JEOL, JSM-6510LV, Japan) was employed to observe the surface characteristics of the PFC membrane and PHA scaffold. Image-Pro Plus (Media Cybernetics, USA) was used to quantitatively measure the fiber diameter distribution of the PFC membranes from the SEM images. Energy-dispersive spectroscopy (EDS; INCA PentaFET ×3, UK) was used to detect the distribution of Ca and P on the surface of the PHA scaffolds. The composition and crystal structure of the PHA scaffolds were analyzed by X-ray diffraction (XRD; DX-2500, China). Fully reflective infrared ray tests of the PFC membranes and PHA scaffolds were analyzed by Fourier transform infrared spectroscopy (FTIR; Nicolet 6700, USA). Thermogravimetric analysis (TG; STA499F3 Jupiter®, Germany) was employed to analyze the thermal stability of the membranes and the scaffolds. The tensile properties of the PFC membranes (a thickness of 0.1–0.2 mm, a width of 4 mm, and a length of 75 mm) and the compressive strengths of the PHA scaffolds (10 mm × 10 mm × 10 mm) were tested using an electronic universal testing machine (AG-IC 50 kN, Japan). The surface wettability of the PFC membranes and the PHA flat membranes was characterized using an instrument that could measure the water contact angle (Chengde Dingsheng, JY-82B, China). Five samples were tested for each type of membrane.

The porosities of the PHA scaffolds were measured by the mass-volume calculation method. The weight (m_0) of the 3D-printed PHA scaffolds (8 mm × 8 mm × 8 mm) was recorded after they were thoroughly dried in a vacuum oven. The weight (m_1) of the pycnometer, which was filled with anhydrous ethanol, was recorded. We immersed the scaffolds in the pycnometer and vacuumized them to fill the pores of the scaffolds with anhydrous ethanol. We then filled the pycnometer and recorded its weight (m_2). Finally, we recorded the weight (m_3) of the pycnometer and anhydrous ethanol after removing the scaffolds. The porosity of the PHA scaffolds was calculated as follows:

$$\text{Porosity} = (m_2 - m_3 - m_0)/(m_1 - m_3) \times 100\%. \quad (1)$$

Interfacial bonding assessment

Vertical stretching and T-peeling tests were employed to evaluate the adhesive intensity between the PFC fibrous membrane and the PHA 3D scaffold in the PFC/PHA-integrated scaffold.

A schematic diagram of vertical stretching is shown in Fig. S1b (Supplementary Information). The PFC membrane of the PFC/PHA-integrated scaffold (10 mm × 10 mm) was fixed to a glass slide, and a load was applied perpendicular to the bond interface to measure the interface adhesive strength.

The T-peeling test evaluated the shear strength of the material according to American Society of Testing Materials (ASTM) Standard F2256, as shown in Fig. S1c (Supplementary Information). The sizes of the adhesive interface, contact surface of the PHA scaffold, PFC membrane, and printing paper were, respectively, 12.5 mm × 15 mm, 12.5 mm × 15 mm, 25 mm × 15 mm, and 25 mm × 15 mm. The PFC membrane and the A4 paper were fixed onto the face and back of the PHA scaffold separately. The other sides of the PFC membrane and paper were clamped to the tensile testing jigs in a T shape. Tensile tests were performed at a stretching rate of 250 mm/min. The adhesive intensity was calculated as follows:

$$\text{Adhesive intensity} = \frac{F_\mathrm{m}}{W}, \quad (2)$$

where F_m is the maximum tensile force of the peeling test and W is the width of the stripping sample.

SEM was used to observe the bonding interface of the PFC/PHA scaffold after brittle fracture under liquid nitrogen and the morphology of the PHA scaffold after the PFC membrane was stripped from the PFC/PHA-integrated scaffold.

In vitro degradation

PFC membranes (Φ 9 mm) and PHA scaffolds (9 mm × 9 mm × 2 mm) were cut, weighed (m_0), and immersed in 4 mL of phosphate-buffered saline (PBS; pH 7.4). Subsequently, all tubes were placed in an incubator shaker at 120 r/min and 37 °C. The incubating media were changed every week. At each predetermined time point, a set of samples were dried to a constant weight in a vacuum oven after they had been rinsed with PBS. The weight loss rate was then calculated.

In vitro cell experiments

The proliferation of bone marrow-derived mesenchymal stem cells (BMSCs) on the PHA scaffold and that of the L929 cells on the PFC membrane were assessed using a cell counting kit-8 (CCK-8) assay (Invitrogen, USA) at desired time points (1, 3, 5, and 7 d). After 4 d of culture, the morphologies of BMSCs on PHA scaffolds and L929 cells on PFC membranes were observed by SEM. After 4 d of culture, the F-actin and nuclei of the cells were stained by phalloidin and Hoechst (Life Technologies, USA), respectively. The viability of cells was then tested by staining the cells with a live/dead working solution (Molecular Probes, USA). Fluorescent images were visualized with a confocal laser scanning microscope (Nikon, A1R, MP^+, Tokyo, Japan).

To investigate the barrier effect of fibrous membranes in the integrated scaffold, the polycarbonate membrane of the Transwell inserts (Corning; 3422) was stripped and replaced by a PFC/PHA-integrated scaffold (with the PHA scaffold located on the downside), which was attached to the Transwell inserts using PLGA paste. The PHA scaffold was set as the control group. L929 cells at a density of 5×10^3 cells/well were seeded into the upper chambers, and after culturing for 4 d, the cells at the lower chambers were stained with crystal violet (Meilun Biological Technology, Dalian, China) to assess the capacity of PFC membranes to prevent cell infiltration.

In vivo assessments of hard/soft tissue regeneration

One-year-old male Beagle dogs weighing approximately 10 kg were used in a study of oral hard and soft tissue defects. The tooth extraction sites are shown in Fig. S2a (Supplementary Information). The groups were set as follows: (1) defects without implantation of materials were set as a sham group (Ctrl group); (2) defects with implanted PFC/PHA-integrated scaffolds were set as an experimental group (PFC/PHA group); (3) defects filled with commercially available Bio-Oss® collagen (GEISTLICH, Switzerland) and then covered by Bio-Gide (GEISTLICH, Switzerland) membranes were set as a positive control group (BGC group).

Before the surgery, the beagles were anesthetized by injecting an appropriate dose (0.1 mL/kg) of pentobarbital (0.03 g/mL) intramuscularly. The surgical procedure of scaffold implantation is shown in Figs. S2b–S2g (Supplementary Information). Split-root techniques were used to extract the mandibular premolars (P2, P3, and P4). Circular defects (Φ 4 mm × 6 mm) were created using a trephine bur. Materials in the same group were implanted into the defects on the same side. Finally, the membranes were fixed with titanium screws, and open soft tissue defects of size 2 mm × 8 mm were fabricated by suturing the soft tissue. After the surgeries, penicillin was injected once a day for three days. The dogs were fed a soft pellet diet during the whole experiment. Body weights were recorded weekly to obtain body weight percent, and the calculation formula was as follows:

$$\text{Body weight percent} = \frac{w}{w_0} \times 100\%, \tag{3}$$

where w is the body weight of the dogs at each time point, and w_0 is the starting weight.

Soft tissue healing was photographed postoperatively at 0, 7, 14, and 28 d. We have drawn on various established methods to provide a comprehensive scoring standard for the assessment of oral soft tissue healing after surgery (Table S1 in Supplementary Information) [25–27]. The beagles were sacrificed after four and eight weeks, and the bone samples were fixed in 4% (volume fraction) paraformaldehyde for further analysis. Before the histological analysis, micro-computed tomography (micro-CT; SCANCO Medical AG, Sweden) with settings of 45 kV and 175 mA was used to evaluate the regenerative condition of the hard tissues within the defect areas. For the histological analysis, the fixed specimens were decalcified. The hematoxylin and eosin (H&E) and Masson's trichrome staining were carried out to examine the bone repair.

Statistical analyses

Statistical analyses were performed using SPSS software. The experimental data were analyzed using the one-way analysis of variance (ANOVA) and Student's t-test. The results were presented as mean ± standard deviation (SD). A value of $p < 0.05$ was considered to be statistically significant. In the graph, the significant difference was defined as $^{*}p < 0.05$, $^{**}p < 0.01$, and $^{***}p < 0.001$.

Results and discussion

Morphology of the PFC membrane and the PHA scaffold

The surface morphology of the PLGA and PFC electrospun fibers is presented in Figs. 1a and 1b. It is evident that the fibers are uniform, smooth, and randomly oriented. The average diameter of the fibers decreased from (1380.68 ± 162.93) nm to (672.39 ± 105.61) nm with the incorporation of FC (Figs. 1c and 1d). This is mainly because the incorporation of FC decreased the viscosity of the electrospinning solution [28]. Previous research has shown that reducing the fiber diameter from micron-size to nanoscale increases the specific surface area and protein adsorption and consequently promotes the aggregation of integrin, which mediates cell adhesion [29–32].

Figure 1e presents the morphology of the PHA scaffolds and shows that the scaffolds have a similar macropore size of approximately 350 μm. Previous studies have proposed that scaffold pores greater than 300 μm are essential for vessel and bone ingrowth, while pores smaller than 300 μm can give rise to chondrification of bone [33–35]. As shown in Fig. 1f, the scaffolds with large amounts of HA show a rough surface that would be beneficial for cell adhesion and migration. The profile image displays the side pores of the scaffolds (Fig. 1g), which would facilitate cell and bone ingrowth, thereby improving interfacial bonding and osteointegration. The PHA scaffolds had a porosity that was estimated to be

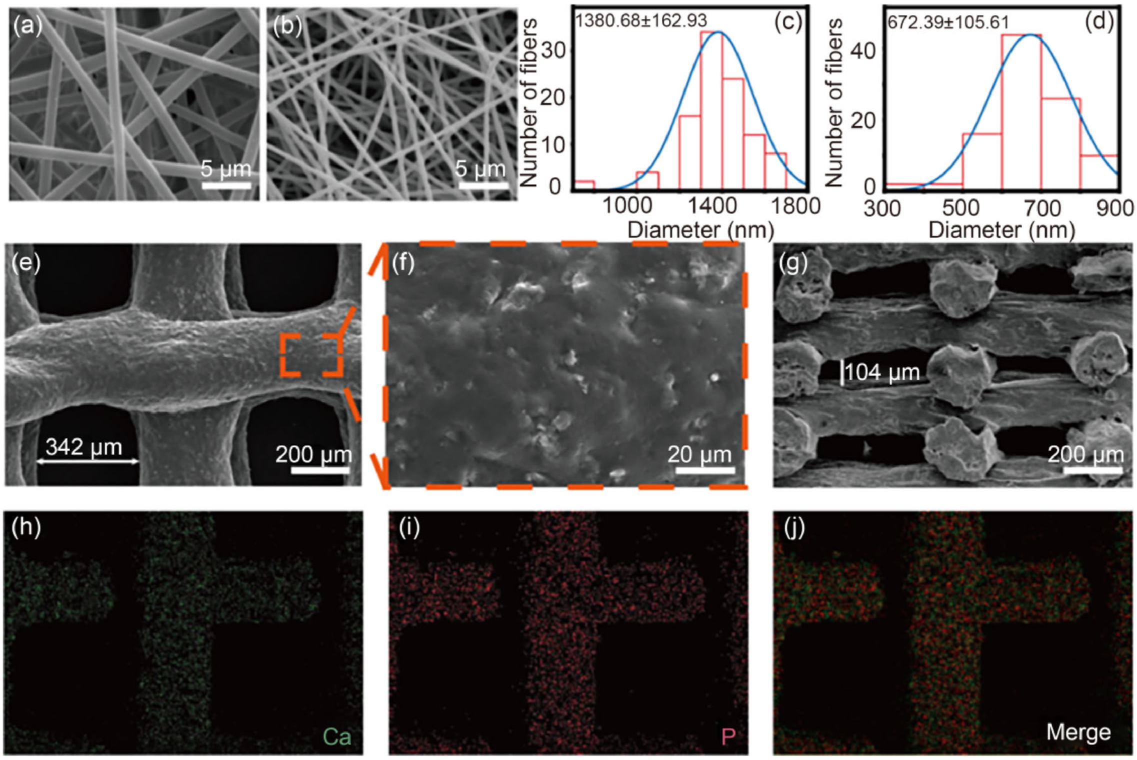

Fig. 1 SEM images of **a** PLGA and **b** PFC membranes with their corresponding diameter distribution (**c** PLGA and **d** PFC). SEM images of the surface (**e**, **f**) and cross section (**g**) of the PHA scaffold. **h**–**j** EDS mapping of Ca and P elements in the PHA scaffold. SEM: scanning electron microscopy; PLGA: poly(lactic-co-glycolic acid); PFC: PLGA and fish collagen (FC) composite; PHA: PLGA and nano-hydroxyapatite; EDS: energy dispersive spectroscopy

(75.05 ± 0.07)%, which is similar to that of human cancellous bone [36] and would be conducive to bone regeneration [37].

Physicochemical characteristics of PFC membrane and PHA scaffold

Homogeneous material composition is key to the uniform and stable mechanical properties of the scaffold. EDS mapping revealed that the PHA scaffolds exhibited a homogeneous distribution of calcium and phosphorus elements (Figs. 1h–1j), indicating that the HA nanoparticles were successfully and uniformly dispersed in the PHA scaffolds. The uniform distribution of HA nanoparticles as an inorganic filler in the PHA scaffolds is likely to prevent unnecessary stress concentration.

The XRD patterns of HA, PLGA, and PHA are shown in Fig. 2a. The diffraction patterns of pure PLGA exhibited enveloped peaks at approximately $2\theta = 19.24°$, which were attributed to the non-crystalline structure of PLGA [38, 39]. The characteristic diffraction peaks of pure HA were observed at 2θ=32.9°, 2θ=31.9°, and 2θ=25.9°. A reduced intensity of the characteristic diffraction peaks of HA was observed in the XRD patterns of PHA due to the wrapping effect of PLGA.

According to the FTIR spectra (Fig. 2b), the absorption bands of the amide I (C = O stretch) and amide II (N–H bending) in FC appear at 1646 and 1538 cm^{-1}, respectively. Meanwhile, these two specific bands of FC were observed for the PFC membrane, although they exhibited a slight shift to lower wavenumbers and appeared at 1645.49 and 1533.6 cm^{-1}, respectively. This could be attributed to the formation of hydrogen bonding between the amino group in the FC and the PLGA molecular chain [40, 41]. The chemical bonds of the HA, PLGA, and PHA scaffold were also identified by FTIR (Fig. 2c). The characteristic absorption peaks of PO_4^{3-} from HA at 603, 565, and 1029 cm^{-1}, along with the characteristic PLGA absorption band (peak of C = O stretching vibration absorption) at 1756.5 cm^{-1} can also be seen in the infrared spectrum of the PHA scaffold [42, 43]. Meanwhile, the characteristic peaks of HA and PLGA showed no significant deviation, indicating that physical blending, rather than a chemical reaction, occurred between PLGA and HA in the PHA scaffold.

According to the TG curves (Fig. 2d), when the temperature rises to 600 °C, the residual mass contents of PLGA and

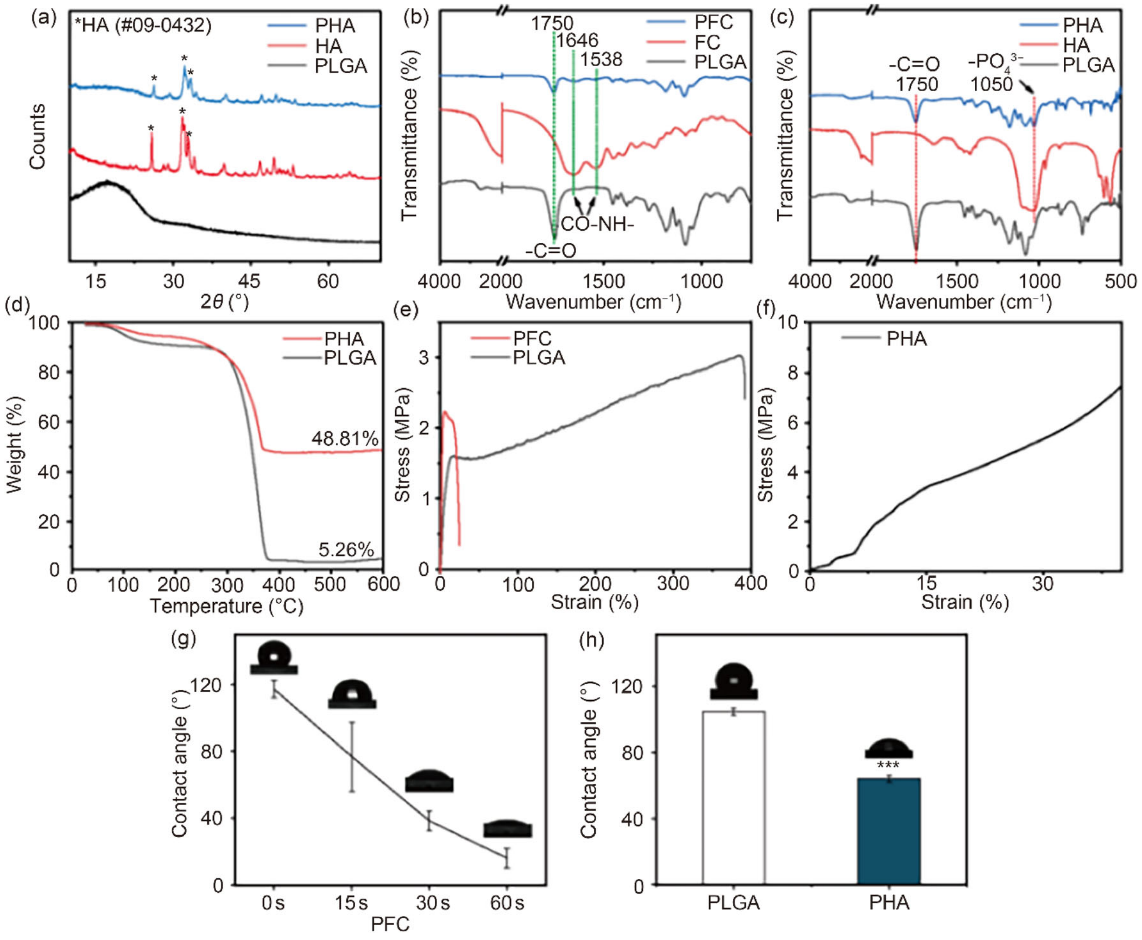

Fig. 2 **a** XRD patterns of PLGA, HA, and PHA. FTIR curves of **b** PLGA, FC, and PFC, and **c** PLGA, HA, and PHA. **d** TG curves of PLGA and PHA. **e** Stress–strain curves of PLGA and PFC membranes. **f** Compressive stress–strain curve of the PHA scaffold. **g** Dynamic water contact angle photos and curve of PFC. **h** The histogram of water contact angle of PLGA and PHA. Data are expressed as mean ± SD ($n = 5$), $^{***}p < 0.001$. XRD: X-ray diffraction; PLGA: poly(lactic-co-glycolic acid); HA: nano-hydroxyapatite; PHA: PLGA and HA; FTIR: Fourier transform infrared spectroscopy; FC: fish collage; PFC: PLGA and FC composite; TG: thermogravimetric analysis; SD: standard deviation

PHA were 5.26% and 48.81%, respectively. The HA content in the PHA scaffolds was basically consistent with the expected HA addition.

Mechanical properties of the PFC membrane and the PHA scaffold

The GTR/GBR membranes were expected to exhibit sufficient mechanical strength to maintain the spatial stability of the in vivo implanting environment. The results of the stress–strain measurement of PFC membranes are shown in Fig. 2e and Table 1. Compared with the pure PLGA membrane, the PFC membrane exhibited superior yield stress and Young's modulus; meanwhile, the elongation at break decreased to (5.50 ± 0.43)%. These results indicate that the incorporation of FC increased the molecular interactions in the membrane, thereby substantially enhancing the mechanical strength of the membrane [16]. Simultaneously, the elastic modulus of the PFC membrane is similar to that of the Bio-Gide membrane (15.7 MPa), and makes the membrane suitable for use as a GTR/GBR membrane [44].

Table 1 Mechanical properties of PLGA and PFC fibrous membranes

Sample	Young's modulus (MPa)	Yield stress (MPa)	Elongation at break (%)
PLGA	7.92 ± 1.74	1.37 ± 0.26	231.59 ± 14.53
PFC	13.36 ± 2.84	2.28 ± 0.49	5.50 ± 0.43

PLGA: poly(lactic-co-glycolic acid); PFC: PLGA and fish collage (FC) composite. Data are expressed as mean ± standard deviation (n=5)

The PHA scaffolds exhibited a compressive strength of (11.52 ± 1.21) MPa, as shown in Fig. 2f, which is close to the compressive strength of human trabecular bone (2–12 MPa) [45] compared with that of Bio-Oss bone graft material (35 MPa) [46].

Hydrophilicity of the PFC membrane and the PHA scaffold

The hydrophilicity of materials is an important factor affecting cell adhesion [47]. The dynamic diversification chart of water contact angles with the PFC membrane is demonstrated in Fig. 2g. The water contact angle on the PFC membrane is 117.2° ± 5.3° when the droplet first makes contact with the fibrous membrane, and it decreases to 13.14° ± 5.9° after one minute. This might have been caused by the large surface areas of the electrospun fibers, which mimic the lotus effect. The surface of a lotus leaf, covered with micron-scale pillars and nanotubes, exhibits superhydrophobicity [48], and this property affected the droplet at the beginning. Subsequently, the water contact angle gradually decreased as the droplet infiltrated the fibrous membrane, which is due to the amine and carboxyl functional groups of FC being available to interact with water molecules [49]. It was evident that the addition of FC significantly increased the water affinity of the membranes. The favorable hydrophilic property enhances protein adsorption on the surface of the material and sequentially improves the interactions between cells and materials [50, 51].

The water contact angle of the PHA flat membrane (62.0° ± 2.0°) was significantly lower than that of the PLGA flat membrane (104.5° ± 2.0°) (Fig. 2h), mostly because the HA exposed to the surface greatly increased the hydrophilicity of the scaffold [52]. Previous research has shown that the protein adsorption capacity of biomaterials is enhanced between the water contact angles of 50° and 60°, which would, in turn, lead to the adhesion of cells to materials [53, 54].

Interfacial bonding between PFC and PHA of PFC/PHA-integrated scaffolds

It can be seen from the digital image of the scaffold (Fig. S1a in Supplementary Information) that the PHA scaffold is tightly combined with the PFC membrane, and the dimensional stability of the PFC membrane can be effectively maintained after it is fixed to the PHA scaffold.

As shown in Fig. 3a, the integrated scaffold with an interfacial size of 10 mm × 10 mm withstood a weight of 500 g and an interfacial tensile stress of more than 5 kPa. The results of the shear strength of the materials are shown in Fig. 3b. At the initial tensile stage, the PFC membrane exhibited typical elastic deformation-plastic yield behavior. After the PFC membrane was peeled from the surface of the PHA scaffold, the stress–strain curve showed an obvious plateau, and the interface toughness was (249.78 ± 17.89) J/m^2. The experimental results showed that the PFC/PHA interface was tightly bonded and could resist a certain degree of tensile stress and shear stress.

The bonding of the PFC/PHA interface was further observed using SEM. The brittle fracture profiles of the PFC/PHA binding interface (Figs. 3c and 3d) showed that the PFC membrane was tightly attached to the surface of the PHA scaffold, and the fibers at the bottom of the PFC membrane were fused with the top layer of the PHA scaffold. After the PFC membrane was peeled off the PFC/PHA scaffold, there was still a large number of spinning fibers on the top of the scaffold, and fiber dissolution was observed at the interface, as shown by the arrows (Figs. 3e and 3f). These results demonstrated the strong interfacial bonding between the fibrous membrane and 3D scaffold of the integrated PFC/PHA scaffold.

Degradation behavior

The optimal time for GTR/GBR membranes to remain stable in vivo is from four weeks to several months [55, 56]. The process of bone healing is complex, and bone tissue typically requires 3–6 months to regain its fundamental functionality [57]. Full restoration of the bone's structure, function, and metabolic processes can take a more extended period: approximately 1–2 years [58]. The degradation time that is suitable for bone grafts is generally 6–12 months [59, 60]. The implanted GTR/GBR membrane must have an appropriate degradation rate, and the bone graft should not lose its mechanical strength prematurely to prevent scaffold collapse and deformation. Therefore, we monitored the variation in the morphology and the loss of mass during the immersion in PBS.

As shown in the degradation quality loss diagram (Fig. 4b), the degradation rate of PFC was observably higher than that of PHA. The morphology of PFC and PHA after degradation was observed by SEM. As is evident from Fig. 4a, a few grooves emerged on the surface of the PFC fibers on Day 14; the grooves were gradually enlarged, and the fibers presented as a porous structure and fracture on Day 28; the pore size continued to increase, and the fiber fracture significantly increased on Day 56; finally, on Day 84, the fiber structure was almost gone, and the fiber was characterized by fibrous membrane fragments and a loss of toughness. This was mainly due to the rapid dissolution behavior of FC. Meanwhile, the dissolved FC formed defect points and increased the contact areas with the PBS solution, which facilitated the membrane degradation. These results indicate that the PFC membrane can effectively maintain its structure and prevent the invasion of soft tissues into the defect area within four weeks, after which it rapidly degrades.

The morphology of the PHA scaffolds did not change significantly during the degradation period of 84 d. This

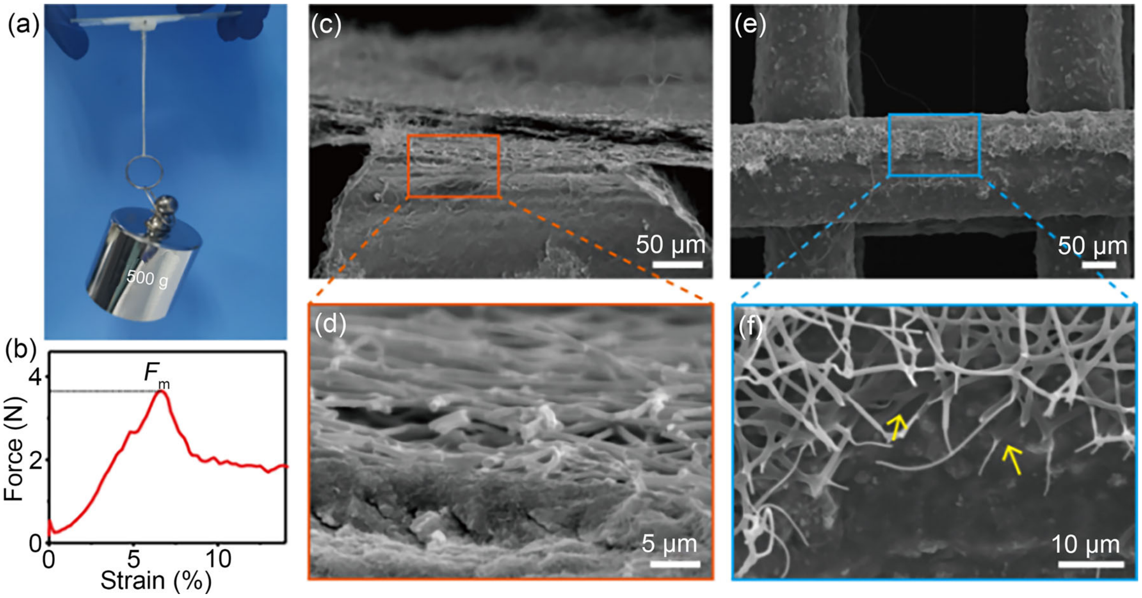

Fig. 3 **a** Digital image of the vertical stretching model. **b** Diagram of stress-force curve of PFC/PHA gradient scaffold. SEM images of **c**, **d** the cross section of PFC/PHA and **e**, **f** surface morphology of PFC/PHA scaffold after the PFC membrane was peeled off (yellow arrows: dissolved PFC fibers on the PHA scaffold). PLGA: poly(lactic-co-glycolic acid); PFC: PLGA and fish collagen (FC) composite; PHA: PLGA and nano-hydroxyapatite; SEM: scanning electron microscopy

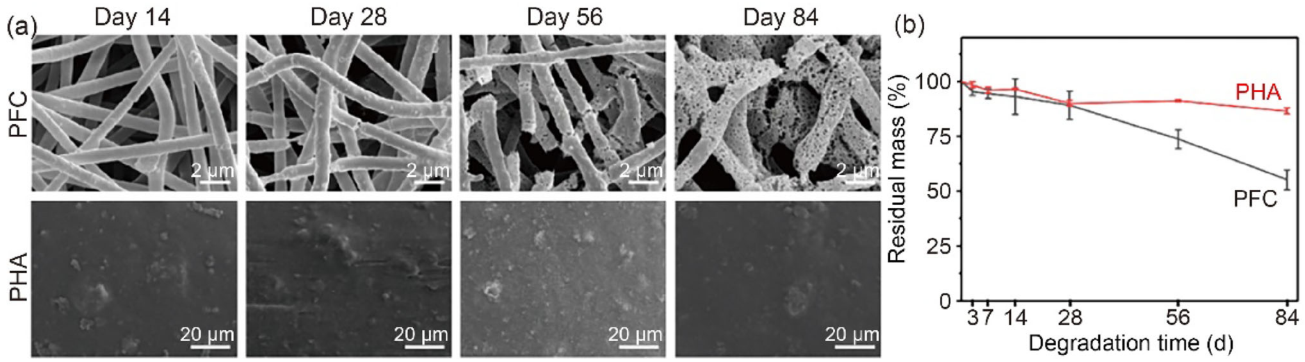

Fig. 4 **a** SEM images of the PFC membrane and the PHA scaffold on Days 14, 28, 56, and 84 during the in vitro degradation time. **b** Residual mass content curves of PFC and PHA over degradation time in vitro. Data are expressed as mean ± SD (*n*=5). SEM: scanning electron microscopy; PLGA: poly(lactic-co-glycolic acid); PFC: PLGA and fish collagen (FC) composite; PHA: PLGA and nano-hydroxyapatite; SD: standard deviation

might have been because, compared with the PFC membrane, the PHA scaffold without a fast-degrading FC had a lower specific surface area available for contacting with the PBS solution. The PHA scaffold degraded at a slower rate, and it was capable of providing mechanical support to the defect area throughout the extended osteogenic process (three months). Another in vivo study from our group [61] has demonstrated that PHA completely degrades within a one-year period of osteogenesis, which aligns with the desired overall degradation profile for scaffolds during the repair process of oral hard and soft tissues. Therefore, the degradation of this material complies with the requirements for integrated scaffold degradation during the repair process for oral hard and soft tissues.

Cell proliferation and morphology

The live/dead staining of L929 on the PFC membrane (Figs. 5a–5c) and BMSCs on the PHA scaffold (Figs. 5d–5f) showed predominantly live cells (green) with very few dead cells (red) on the materials, indicating that the materials were not cytotoxic. The proliferation of BMSCs and L929 on various materials was assessed by CCK-8. The optical density (OD) values increased on Days 4 and 7, indicating that the

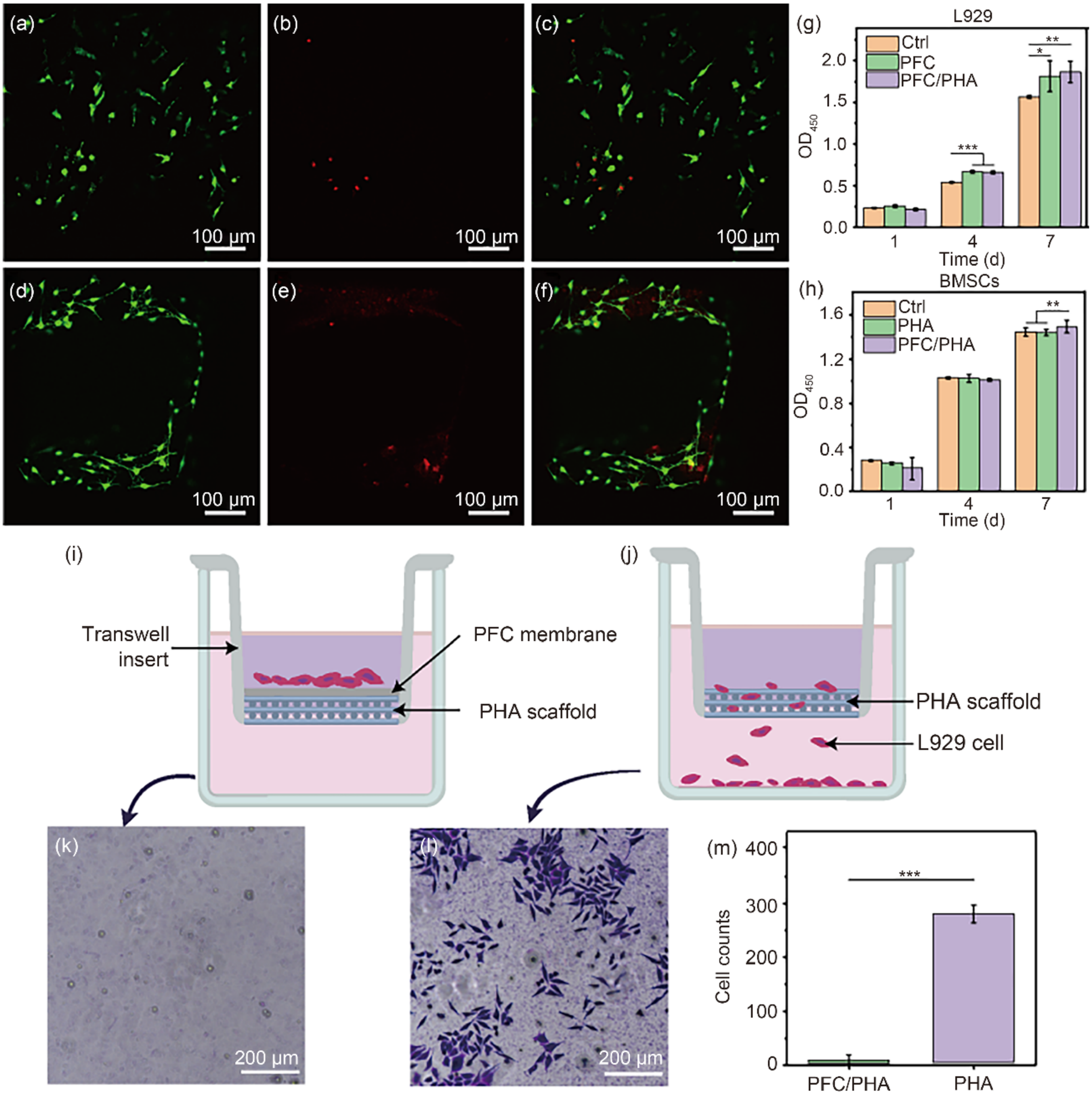

Fig. 5 Live/dead fluorescent images of **a**–**c** L929 cultured on PFC and **d**–**f** BMSCs cultured on PHA for 4 d. Proliferation of **g** L929 and **h** BMSCs on the scaffolds (OD_{450}: optical density at 450 nm). Schematic diagrams of barrier model for **i** PFC/PHA and **j** PHA scaffolds. Micrographs of the lower compartments of **k** the PFC/PHA and **l** the PHA groups. Data are expressed as mean ± SD (n=3); $^{***}p < 0.001$, $^{**}p < 0.01$, and $^{*}p < 0.05$. **m** Cell count of the lower compartment of the PFC/PHA and the PHA groups. PLGA: poly(lactic-co-glycolic acid); PFC: PLGA and fish collage (FC) composite; PHA: PLGA and nano-hydroxyapatite; BMSCs: bone marrow-derived mesenchymal stem cells; SD: standard deviation

membrane or scaffold exerted no significant side effects on cell proliferation. For L929, there were no significant differences in OD values between the control (Ctrl), PHA, and PFC/PHA groups after 1 d of culture (Fig. 5g), whereas the OD values of the PHA and PFC/PHA groups were obviously higher than those in the Ctrl group after 4 and 7 d of culture. This might have been caused by the high specific surface area and ECM-like structure of the PFC membrane, which was able to enhance the proliferation of L929 cells [62]. Meanwhile, FC enhanced cell proliferation. For BMSCs, there were no significant differences between the OD values of the Ctrl, PHA, and PFC/PHA groups after 1 and 4 d of culture (Fig. 5h). The OD value of the PFC/PHA group was significantly higher than those of the PHA and Ctrl groups after 7 d of culture. This could be due to the incorporation of FC with a large number of hydroxyl, carboxyl, and amino groups, which are conducive to cell proliferation [63, 64]. The results showed that BMSCs on the surface of PHA scaffolds and L929 on the surface of PFC membranes had good cytocompatibility.

The fluorescent micrographs illustrated the expression of actin (red) and the distribution of 4′,6-diamidino-2-phenylindole (DAPI)-stained cell nuclei (blue) after 4 d of culture (Figs. S3a–S3c, S3e–S3g in Supplementary Information). As shown in the figures, cells were well-grown with plump morphology and abundant actin, and round or elliptic nuclei, indicating that the PFC membrane and PHA scaffold had no adverse effect on the L929 cells or BMSCs. SEM was also used to observe the cell morphology of the L929 cells and BMSCs after culturing for 4 d. The L929 cells were closely attached to the surface of the PFC membrane in an elongated or polygonal morphology (Fig. S3d in Supplementary Information). Some cells infiltrated into the fibrous membrane and formed anchor-like structures that went deep between the fibers. The cells were interconnected by numerous filopodia. Spindle BMSCs were tiled on the scaffold and were stuck to the rough surface of the PHA scaffold, climbing and growing in all directions with a large number of filopodia (Fig. S3h in Supplementary Information). These results indicated that the PFC membrane and PHA scaffold were able to promote cell adhesion and growth.

The GTR/GBR membrane acts as a barrier to prevent the rapid growth of soft tissue from invading the defect area of the bone, thereby to ensure space for bone regeneration. In the Transwell experiment, we did not observe infiltrated L929 cells on the lower chamber of the Transwell plate in the PFC/PHA group after 4 d of culture (Figs. 5i and 5k), whereas a large number of L929 cells were observed in the PHA group (Figs. 5j and 5l). This difference was statistically significant (Fig. 5m). These results indicate that the PFC electrospun membrane of the PFC/PHA integrated scaffold can effectively prevent L929 penetration and thereby may successfully isolate periodontal defects from the soft tissues.

Hard/soft tissue regeneration in dog mouth

As classic commercially available materials, Bio-Gide collagen and Bio-Oss® collagen are widely recognized for their well-established biocompatibility, and their combined application is commonly utilized in dentistry [65, 66]. Therefore, we employed the combined application of these materials as a positive control group (BGC) to compare its biocompatibility and functionality with our designed integrated porous scaffold (PFC/PHA).

Postoperative observation

The postoperative activity and feeding of the beagles were normal, and neither allergic nor toxic reactions were observed. As shown in Fig. 6b, the weight ratio of the beagles increased slightly, indicating that the experiments had no significant adverse effects on the survival or the life of the animals.

Evaluations of soft tissue regeneration

The healing of the soft tissues is shown in Fig. 6a; no infection occurred in the beagles. No soft tissue healing was observed on Day 7. On Day 14, only P2 in the Ctrl group had healed completely. On Day 28, PFC/PHA and BGC were completely healed, while there was still a white defect in P4 of the Ctrl group. This might have been due to the individual differences between the experimental animals, such as chewing habits, personality, and postoperative habits. As depicted in Fig. 6c, the soft tissue healing scores revealed that both the PFC/PHA and BGC groups achieved the maximum score of six points by the 28th day, which suggests that there was no significant difference in the capacity of PFC/PHA and BGC to guide soft tissue regeneration. Masson's trichrome staining on Day 28 at the wound sites indicated good soft tissue repair across all groups, with no significant inflammation observed (Fig. 6d).

Micro-CT analysis

The new bone formation and the spatial structure of bone trabecula at four and eight weeks postoperation were evaluated by micro-CT analysis. Four weeks after surgery, the new bone had integrated within the scaffolds in the BGC group (Figs. 7c and 7f), whereas the osteogenic effects were not obvious in the Ctrl and PFC/PHA groups (Figs. 7a and 7b). Only a small amount of newly formed bone ingrowth was observed in the defects of the Ctrl and PFC/PHA groups, and the boundary of the hard tissue defect was still clearly visible in a sectional view (Figs. 7d and 7e). The quantitative results showed that the fraction of new bone volume to total volume (BV/TV) in the BGC group was significantly higher than those in the Ctrl and PFC/PHA groups (Fig. 7s). This might have been due to

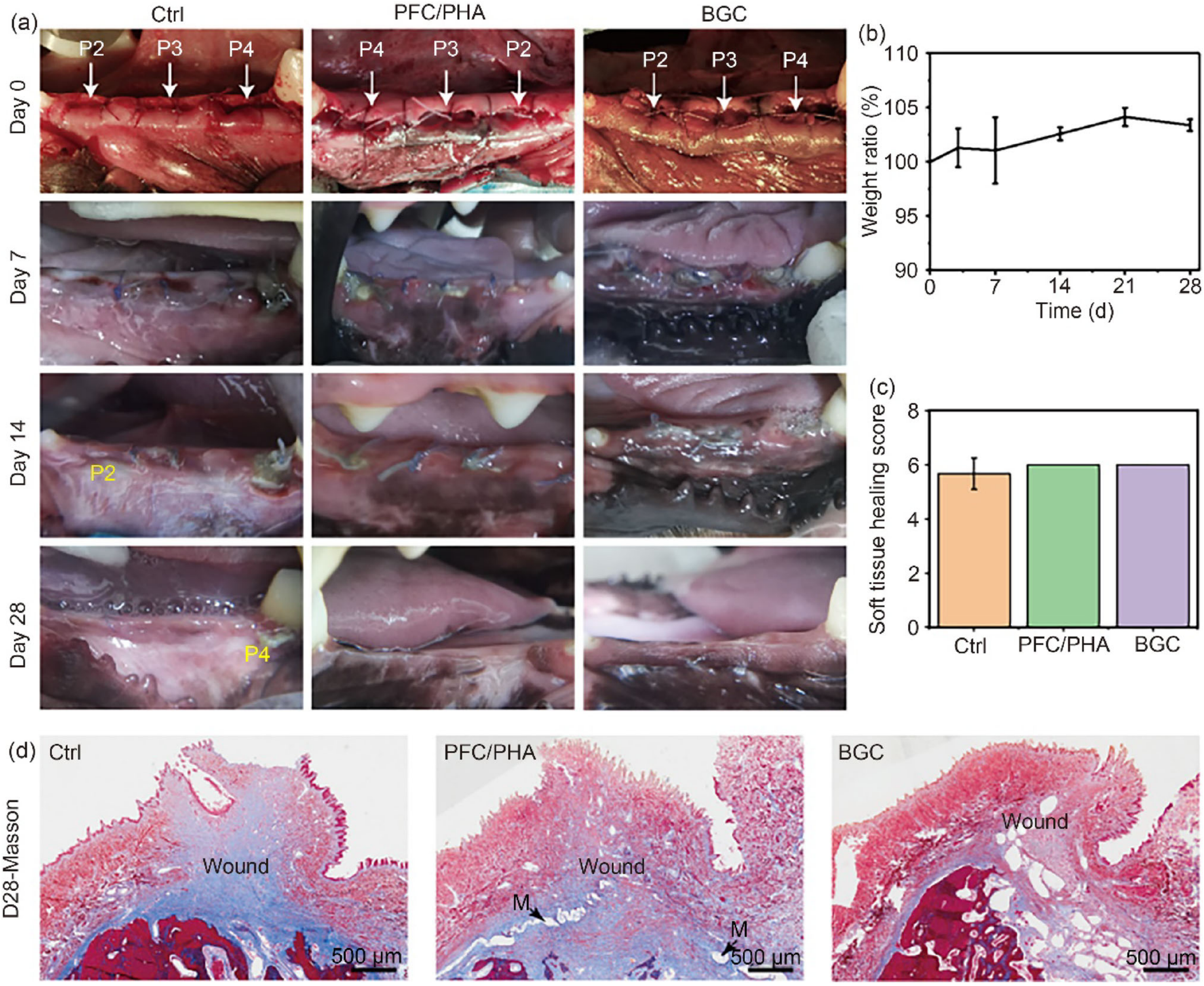

Fig. 6 **a** Digital images of soft tissue healing at predetermined time points. **b** Weight ratio curves for beagles after surgery. **c** Evaluation of soft tissue healing on Day 28. **d** Masson staining of the soft tissue wounds on Day 28. Data are expressed as mean ± SD ($n = 3$). Ctrl: control; PLGA: poly(lactic-co-glycolic acid); PFC: PLGA and fish collage (FC) composite; PHA: PLGA and nano-hydroxyapatite; BGC: defects filled with commercially available Bio-Oss® collagen and then covered by Bio-Gide membranes; M: PFC membrane; SD: standard deviation

the strong development of Bio-Oss bovine bone in Bio-Oss® collagen during micro-CT scanning. There were no significant differences in trabecular number (Tb.N) or trabecular separation (Tb.Sp) among the three groups (Figs. 7t and 7u). After eight weeks, new bone grew into the internal pores of the scaffold, and a visible callus formed in the PFC/PHA group (Fig. 7k). The bottom of the defect boundary was still clearly distinguishable in the Ctrl group (Fig. 7m), whereas the boundary was blurred, and new bone basically occupied the defect area in the PFC/PHA and BGC groups (Figs. 7n and 7o). The quantitative results showed that the new bone increased and thickened in each group, and the BV/TV value increased significantly (Fig. 7s). The BV/TV and Tb.N values of the BGC group were significantly higher than those of the Ctrl group, but the difference between the PFC/PHA and BGC groups was not statistically significant (Figs. 7s and 7t). There were no significant differences in Tb.Sp among the three groups (Fig. 7u). The new bone tissue penetrated the scaffold from the edge of the defect in the PFC/PHA group, which indicated that the porous structure of the PFC/PHA integrated porous scaffold was conducive to the penetrating growth of new bone tissue and had a positive effect on the regeneration of bone tissue.

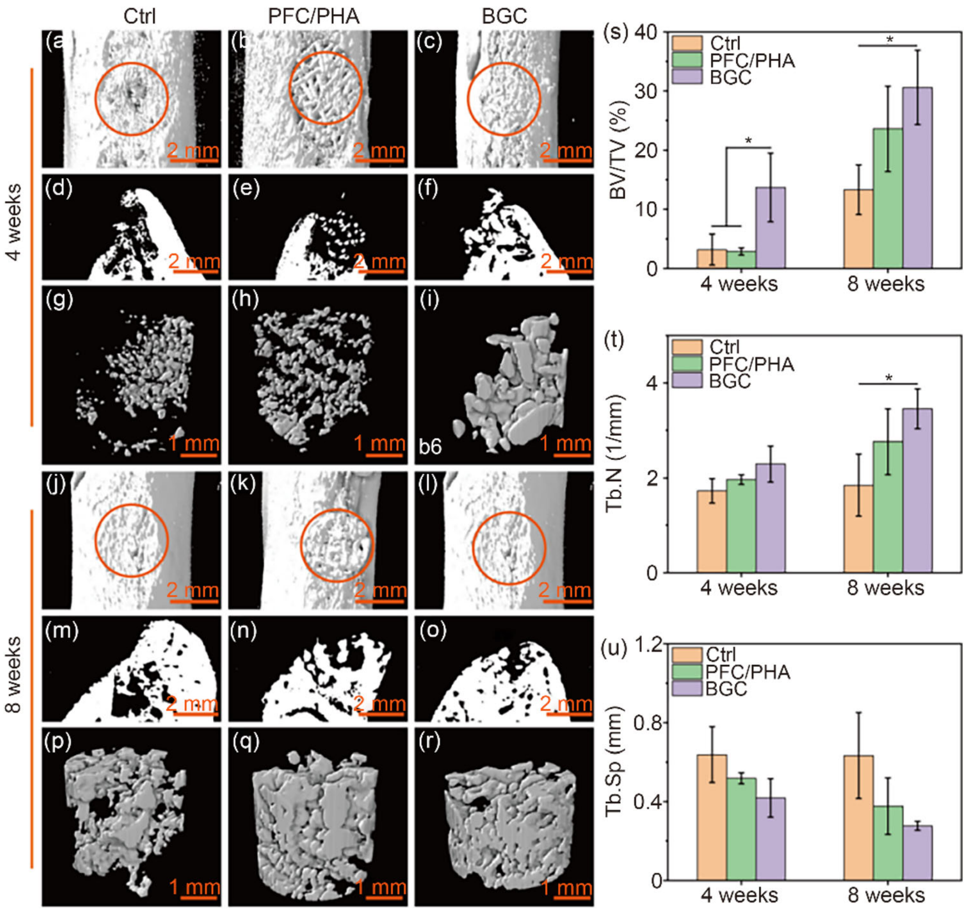

Fig. 7 **a**–**c**, **j**–**l** Micro-CT reconstruction images and **d**–**f**, **m**–**o** their representative monolayers of the mandible defects model at four and eight weeks postimplantation (orange circle: bone defect). **g**–**i**, **p**–**r** 3D micro-CT reconstruction images of new bone tissue. Quantitative analysis of **s** BV/TV, **t** Tb.N, and **u** Tb.Sp. Data are expressed as mean ± SD, $n = 3$, $^{*}p < 0.05$. CT: computed tomography; BV/TV: the fraction of new bone volume to total volume; Tb.N: trabecular number; Tb.Sp: trabecular separation; SD: standard deviation; Ctrl: control; PLGA: poly(lactic-co-glycolic acid); PFC: PLGA and fish collage (FC) composite; PHA: PLGA and nano-hydroxyapatite; BGC: defects filled with commercially available Bio-Oss® collagen and then covered by Bio-Gide membranes

Histological analysis

In addition, we performed a histological analysis of the defect area to investigate the ability of the PFC/PHA in preventing unwanted fibrous tissue invasion and in guiding bone tissue regeneration. H&E and Masson staining of the control group at four weeks (Fig. 8) showed that there was a large amount of soft tissue occupying the defect area. It has been reported that four weeks after subcutaneous implantation, the thickness of the Bio-Gide membrane decreases, accompanied by an almost complete biodegradation [67, 68]. From our stained sections, it can also be observed that the Bio-Gide membrane was almost completely degraded before the healing of the bone defect, which would allow soft tissue to grow into the defect area. In contrast, the PFC/PHA group showed clear evidence of the PFC membrane, an increased number of new blood vessels (indicated by yellow stars), and a greater amount of new bone formation.

At eight weeks postoperation, the Ctrl group showed significant bone wall collapse, and only a small amount of new bone was found in the defect area. Due to early membrane degradation, fibrous tissue had invaded the bone defect area, which resulted in the defect area of the BGC group not being fully filled with new bone. Conversely, the PFC membrane was still partially present, and no fibrous tissue invasion was observed in the defect area of the PFC/PHA group; instead, the defect area was filled with new bone (Fig. 9).

These results showed that the relatively dense PFC fibrous membrane of the integrated scaffold could effectively prevent fibrous connective tissue from invading the defect area, and the porous 3D scaffold of the integrated scaffold could support the bone wall, thereby providing a stable space for bone regeneration. These results indicated that the integrated scaffolds prepared in this study have great application potential in the field of alveolar bone augmentation, especially in the repair of large jaw defects.

Conclusions

To meet the needs of regeneration and the functional reconstruction of large soft and hard tissue defects in the oral cavity, we developed an integrated gradient porous scaffold (PFC/PHA) by combining an ECM-like PFC electrospinning membrane with a 3D-printed PHA scaffold. Because we used

Fig. 8 Histological analysis of the samples from beagle alveolar bones at four weeks postimplantation. Row 1: Overall observation of the samples by H&E staining. Row 2: Magnified view of the blue box regions in row 1 (20×). Row 3: Masson staining of the blue box regions in row 1 (20×). Row 4: Magnified view of the red box regions in row 2 (100×). Row 5: Masson staining of the red box regions in row 3 (100×). Ctrl: control; PLGA: poly(lactic-co-glycolic acid); PFC: PLGA and fish collage (FC) composite; PHA: PLGA and nano-hydroxyapatite; BGC: defects filled with commercially available Bio-Oss® collagen and then covered by Bio-Gide membranes; S: PHA scaffold; M: PFC membrane; O: Bio-Oss®; NB: new bone; MB: mature bone; FT: fibrous tissue; asterisks represent blood vessels

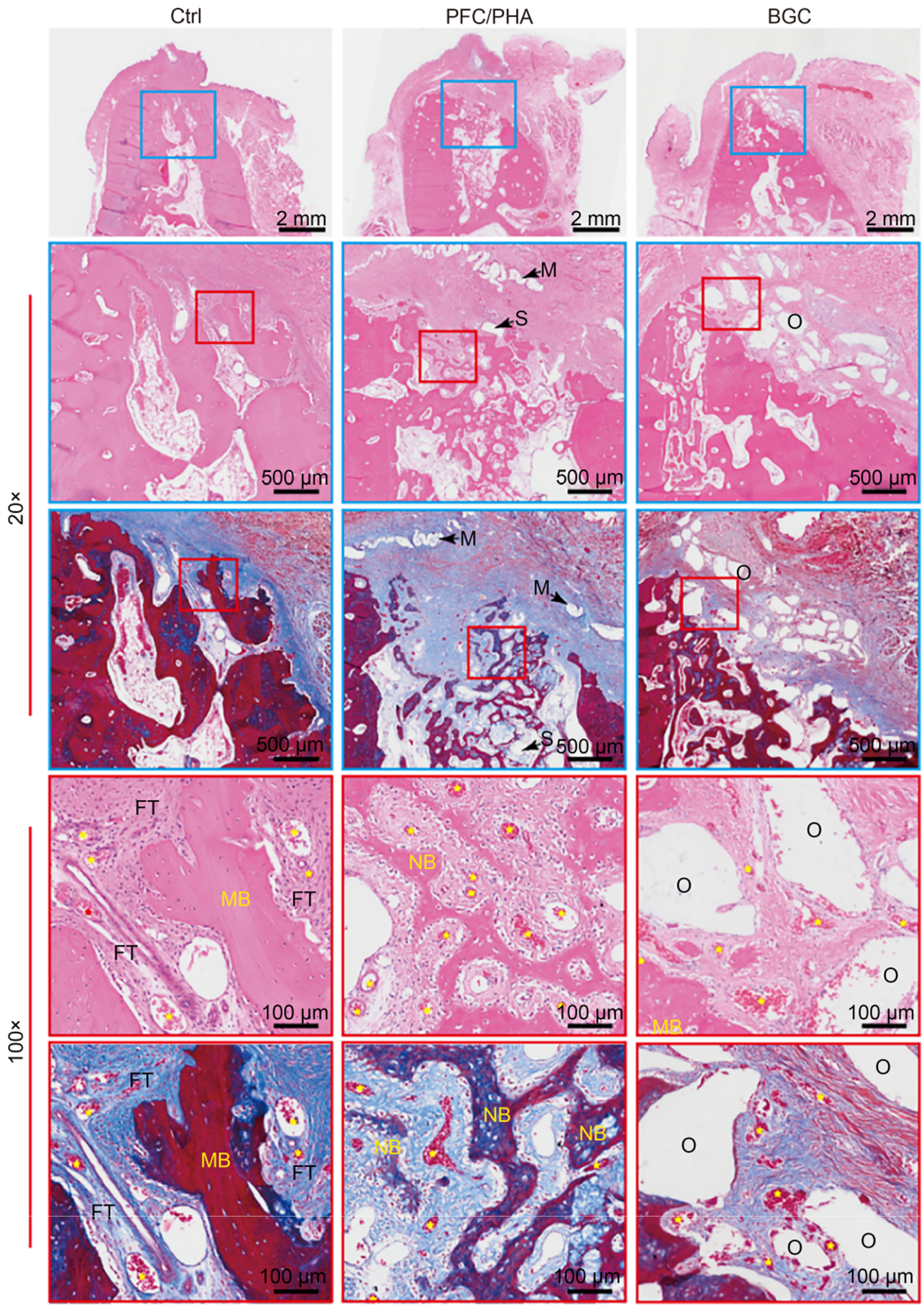

the same PLGA composition for the upper PFC fibrous membrane and the lower PHA 3D scaffold, the membrane and the scaffold formed a strong interface bond that was able to resist some degrees of tensile stress and shear stress. Our in vitro degradation experiments showed that the upper PFC membrane degraded faster than the lower PHA scaffold, which aligns with the respective needs of oral soft and hard tissue repair. The in vitro cell experiments demonstrated that the PFC/PHA scaffold could promote the proliferation of BMSCs and L929 without adverse effects on cell structure, viability, or adhesion. Importantly, the PFC membrane could effectively prevent L929 cells from infiltrating the bone scaffold area. We further established a model of oral soft and hard tissue defects in beagles after tooth extraction and then implanted the PFC/PHA scaffold. CT and histological analyses at four and eight weeks confirmed that the PFC/PHA scaffold effectively prevented unwanted fibrous tissue invasion and promoted the healing of oral soft tissues and the regeneration of hard tissues. These results demonstrate that the developed integrated scaffold shows great promise in

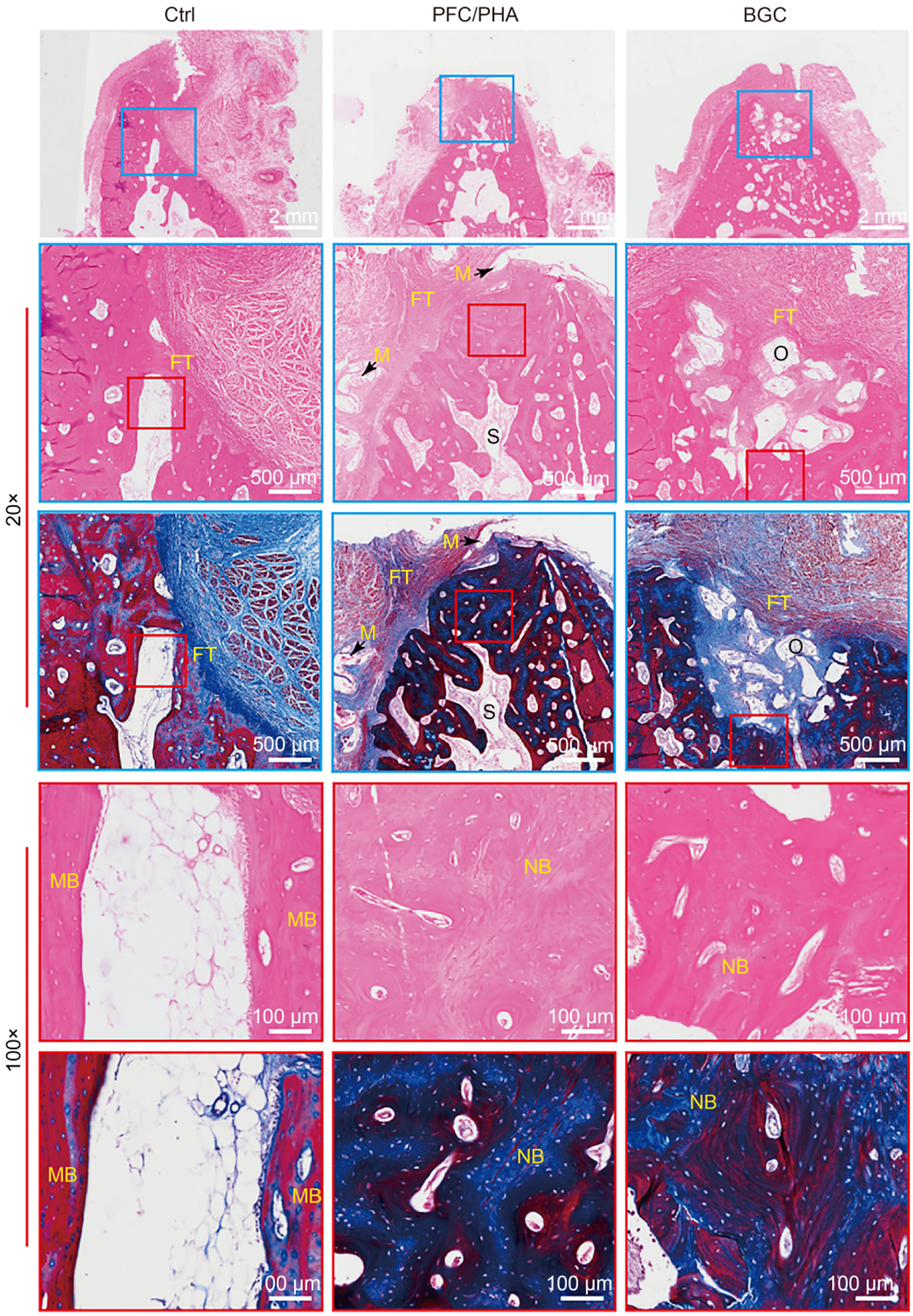

Fig. 9 Histological analysis of the samples from beagle alveolar bones at eight weeks postimplantation. Row 1: Overall observation of the samples by H&E staining. Row 2: Magnified view of the blue box regions in row 1 (20×). Row 3: Masson staining of the blue box regions in row 1 (20×). Row 4: Magnified view of the red box regions in row 2 (100×). Row 5: Masson staining of the red box regions in row 3 (100×). Ctrl: control; PLGA: poly(lactic-co-glycolic acid); PFC: PLGA and fish collage (FC) composite; PHA: PLGA and nano-hydroxyapatite; BGC: defects filled with commercially available Bio-Oss® collagen and then covered by Bio-Gide membranes; S: PHA scaffold; M: PFC membrane; O: Bio-Oss®; NB: new bone; MB: mature bone; FT: fibrous tissue

guiding the regeneration and reconstruction of large soft and hard tissues in the oral cavity.

Supplementary Information The online version contains supplementary material available at https://doi.org/10.1007/s42242-024-00311-4.

Acknowledgements This work was supported by the National Natural Science Foundation of China (No. 32371398), the Sichuan International Science and Technology Innovation Cooperation Project, China (No. 2023YFH0064), the National Key Research and Development Program of China (No. 2016YFA0201700), and the Fundamental Research Funds for the Central Universities, China. We would like to thank Dr. Li Chen from Analytical and Testing Center, Sichuan University for the help with micro-CT analysis.

Author contributions LY and CY contributed to investigation, data curation, writing–original draft, formal analysis, visualization. JWW helped in methodology, data curation, validation, writing–review & editing. SEJ helped in methodology, data curation, validation. YZ and XJL helped in supervision and project administration. YBL contributed to conceptualization and funding acquisition. JDL contributed to conceptualization, funding acquisition, writing–review & editing.

Declarations

Conflict of interest The authors declare that they have no conflict of interest.

Ethical approval All animal-related experiments in this study followed the National Institutes of Health (NIH) Guide for the Care and Use of Laboratory Animals and approved by the Ethics Committee of West China Hospital of Sichuan University (Ethical No. 2020253A).

References

1. Slots J (2022) Concise evaluation and therapeutic guidelines for severe periodontitis: a public health perspective. Periodontol 2000 90(1):262–265. https://doi.org/10.1111/prd.12463
2. Peres MA, Macpherson LMD, Weyant RJ et al (2019) Oral diseases: a global public health challenge. Lancet 394(10194):249–260. https://doi.org/10.1016/s0140-6736(19)31146-8
3. Kijartorn P, Wongpairojpanich J, Thammarakcharoen F et al (2022) Clinical evaluation of 3D printed nano-porous hydroxyapatite bone graft for alveolar ridge preservation: a randomized controlled trial. J Dent Sci 17(1):194–203. https://doi.org/10.1016/j.jds.2021.05.003
4. Sheikh Z, Hamdan N, Ikeda Y et al (2017) Natural graft tissues and synthetic biomaterials for periodontal and alveolar bone reconstructive applications: a review. Biomater Res 21(1):9. https://doi.org/10.1186/s40824-017-0095-5
5. Chappuis V, Rahman L, Buser R et al (2017) Effectiveness of contour augmentation with guided bone regeneration: 10-year results. J Dent Res 97(3):266–274. https://doi.org/10.1177/0022034517737755
6. Mertens C, Braun S, Krisam J et al (2019) The influence of wound closure on graft stability: an in vitro comparison of different bone grafting techniques for the treatment of one-wall horizontal bone defects. Clin Implant Dent Relat Res 21(2):284–291. https://doi.org/10.1111/cid.12728
7. Jung UW, Lee JS, Park WY et al (2011) Periodontal regenerative effect of a bovine hydroxyapatite/collagen block in one-wall intrabony defects in dogs: a histometric analysis. J Periodontal Implant Sci 41(6):285–292. https://doi.org/10.5051/jpis.2011.41.6.285
8. Bottino MC, Thomas V, Schmidt G et al (2012) Recent advances in the development of GTR/GBR membranes for periodontal regeneration—a materials perspective. Dent Mater 28(7):703–721. https://doi.org/10.1016/j.dental.2012.04.022
9. Ul Hassan S, Bilal B, Nazir MS et al (2021) Recent progress in materials development and biological properties of GTR membranes for periodontal regeneration. Chem Biol Drug Des 98(6):1007–1024. https://doi.org/10.1111/cbdd.13959
10. Hoogeveen EJ, Gielkens PFM, Schortinghuis J et al (2009) Vivosorb® as a barrier membrane in rat mandibular defects. An evaluation with transversal microradiography. Int J Oral Maxillofac Surg 38(8):870–875. https://doi.org/10.1016/j.ijom.2009.04.002
11. Doeri F, Huszar T, Nikolidakis D et al (2007) Effect of platelet-rich plasma on the healing of intra-bony defects treated with a natural bone mineral and a collagen membrane. J Clin Periodontol 34(3):254–261. https://doi.org/10.1111/j.1600-051X.2006.01044.x
12. Hassanbhai AM, Lau CS, Wen F et al (2017) In vivo immune responses of cross-linked electrospun tilapia collagen membrane. Tissue Eng Part A 23(19–20):1110–1119. https://doi.org/10.1089/ten.tea.2016.0504
13. Makadia HK, Siegel SJ (2011) Poly lactic-co-glycolic acid (PLGA) as biodegradable controlled drug delivery carrier. Polymers 3(3):1377–1397. https://doi.org/10.3390/polym3031377
14. Lim YS, Ok YJ, Hwang SY et al (2019) Marine collagen as a promising biomaterial for biomedical applications. Mar Drugs 17(8):467. https://doi.org/10.3390/md17080467
15. Hoyer B, Bernhardt A, Lode A et al (2014) Jellyfish collagen scaffolds for cartilage tissue engineering. Acta Biomater 10(2):883–892. https://doi.org/10.1016/j.actbio.2013.10.022
16. Jin SE, Sun FH, Zou Q et al (2019) Fish collagen and hydroxyapatite reinforced poly(lactide-co-glycolide) fibrous membrane for guided bone regeneration. Biomacromol 20(5):2058–2067. https://doi.org/10.1021/acs.biomac.9b00267
17. Jin SE, Yang RL, Chu CY et al (2021) Topological structure of electrospun membrane regulates immune response, angiogenesis and bone regeneration. Acta Biomater 129:148–158. https://doi.org/10.1016/j.actbio.2021.05.042
18. Hu C, Chu CY, Liu L et al (2021) Dissecting the microenvironment around biosynthetic scaffolds in murine skin wound healing. Sci Adv 7(22):eabf0787. https://doi.org/10.1126/sciadv.abf0787
19. Lian MF, Han Y, Sun BB et al (2020) A multifunctional electrowritten bi-layered scaffold for guided bone regeneration. Acta Biomater 118:83–99. https://doi.org/10.1016/j.actbio.2020.08.017
20. Liu J, Zou Q, Wang CX et al (2021) Electrospinning and 3D printed hybrid bi-layer scaffold for guided bone regeneration. Mater Des 210:110047. https://doi.org/10.1016/j.matdes.2021.110047
21. Dou YC, Huang JH, Xia X et al (2021) A hierarchical scaffold with a highly pore-interconnective 3D printed PLGA/n-HA framework and an extracellular matrix like gelatin network filler for bone regeneration. J Mater Chem B 9(22):4488–4501. https://doi.org/10.1039/d1tb00662b
22. Xia X, Huang JH, Wei JW et al (2022) Magnesium oxide regulates the degradation behaviors and improves the osteogenesis of poly(lactide-co-glycolide) composite scaffolds. Compos Sci Technol 222:109368. https://doi.org/10.1016/j.compscitech.2022.109368
23. Wei JW, Xia X, Xiao SQ et al (2023) Sequential dual-biofactor release from the scaffold of mesoporous HA microspheres and PLGA matrix for boosting endogenous bone regeneration. Adv Healthcare Mater 12(20):e2300624. https://doi.org/10.1002/adhm.202300624
24. Li LM, Zuo Y, Zou Q et al (2015) Hierarchical structure and mechanical improvement of an n-HA/GCO-PU composite scaffold for bone regeneration. ACS Appl Mater Interfaces 7(40):22618–22629. https://doi.org/10.1021/acsami.5b07327
25. Hagenaars S, Louwerse PHG, Timmerman MF et al (2004) Soft-tissue wound healing following periodontal surgery and Emdogain® application. J Clin Periodontol 31(10):850–856. https://doi.org/10.1111/j.1600-051x.2004.00571.x
26. Tonetti MS, Fourmousis I, Suvan J et al (2004) Healing, post-operative morbidity and patient perception of outcomes following regenerative therapy of deep intrabony defects. J Clin Periodontol 31(12):1092–1098. https://doi.org/10.1111/j.1600-051x.2004.00615.x
27. Huang LH, Neiva REF, Wang HL (2005) Factors affecting the outcomes of coronally advanced flap root coverage procedure. J Periodontol 76(10):1729–1734. https://doi.org/10.1902/jop.2005.76.10.1729
28. Jin SE, Gao J, Yang RL et al (2022) A baicalin-loaded coaxial nanofiber scaffold regulated inflammation and osteoclast differentiation for vascularized bone regeneration. Bioact Mater 8:559–572. https://doi.org/10.1016/j.bioactmat.2021.06.028
29. Irvine DJ, Hue KA, Mayes AM et al (2002) Simulations of cell-surface integrin binding to nanoscale-clustered adhesion ligands. Biophys J 82(1):120–132. https://doi.org/10.1016/S0006-3495(02)75379-4

30. ter Brugge PJ, Torensma R, De Ruijter JE et al (2002) Modulation of integrin expression on rat bone marrow cells by substrates with different surface characteristics. Tissue Eng 8(4):615–626. https://doi.org/10.1089/107632702760240535
31. Yang K, Jung H, Lee HR et al (2014) Multiscale, hierarchically patterned topography for directing human neural stem cells into functional neurons. ACS Nano 8(8):7809–7822. https://doi.org/10.1021/nn501182f
32. Yao X, Peng R, Ding JD (2013) Cell-material interactions revealed via material techniques of surface patterning. Adv Mater 25(37):5257–5286. https://doi.org/10.1002/adma.201301762
33. Matsiko A, Gleeson JP, O'Brien FJ (2015) Scaffold mean pore size influences mesenchymal stem cell chondrogenic differentiation and matrix deposition. Tissue Eng Part A 21(3–4):486–497. https://doi.org/10.1089/ten.tea.2013.0545
34. Tan XP, Tan YJ, Chow CSL et al (2017) Metallic powder-bed based 3D printing of cellular scaffolds for orthopaedic implants: a state-of-the-art review on manufacturing, topological design, mechanical properties and biocompatibility. Mater Sci Eng C 76:1328–1343. https://doi.org/10.1016/j.msec.2017.02.094
35. Dziaduszewska M, Zieliński A (2021) Structural and material determinants influencing the behavior of porous Ti and its alloys made by additive manufacturing techniques for biomedical applications. Materials 14(4):712. https://doi.org/10.3390/ma14040712
36. Liu JJ, Lan L, Zhou JF et al (2019) Influence of cancellous bone microstructure on ultrasonic attenuation: a theoretical prediction. Biomed Eng Online 18(1):103. https://doi.org/10.1186/s12938-019-0724-4
37. Hing KA (2005) Bioceramic bone graft substitutes: influence of porosity and chemistry. Int J Appl Ceram Technol 2(3):184–199. https://doi.org/10.1111/j.1744-7402.2005.02020.x
38. Kim HK, Park TG (2004) Comparative study on sustained release of human growth hormone from semi-crystalline poly(L-lactic acid) and amorphous poly(D, L-lactic-co-glycolic acid) microspheres: morphological effect on protein release. J Contr Rel 98(1):115–125. https://doi.org/10.1016/j.jconrel.2004.04.020
39. Tavakoli E, Mehdikhani-Nahrkhalaji M, Hashemi-Beni B et al (2015) Preparation, characterization and mechanical assessment of poly (lactide-co-glycolide)/ hyaluronic acid/ fibrin/ bioactive glass nano-composite scaffolds for cartilage tissue engineering applications. Procedia Mater Sci 11:124–130. https://doi.org/10.1016/j.mspro.2015.11.126
40. Heu MS, Lee JH, Kim HJ et al (2010) Characterization of acid- and pepsin-soluble collagens from flatfish skin. Food Sci Biotechnol 19(1):27–33. https://doi.org/10.1007/s10068-010-0004-3
41. Zou Y, Wang L, Cai PP et al (2017) Effect of ultrasound assisted extraction on the physicochemical and functional properties of collagen from soft-shelled turtle calipash. Int J Biol Macromol 105(Pt 3):1602–1610. https://doi.org/10.1016/j.ijbiomac.2017.03.011
42. Rapacz-Kmita A, Paluszkiewicz C, Slosarczyk A et al (2005) FTIR and XRD investigations on the thermal stability of hydroxyapatite during hot pressing and pressureless sintering processes. J Mol Struct 744:653–656. https://doi.org/10.1016/j.molstruc.2004.11.070
43. Kang BS, Choi JS, Lee SE et al (2017) Enhancing the in vitro anticancer activity of albendazole incorporated into chitosan-coated PLGA nanoparticles. Carbohydr Polym 159:39–47. https://doi.org/10.1016/j.carbpol.2016.12.009
44. Ortolani E, Quadrini F, Bellisario D et al (2015) Mechanical qualification of collagen membranes used in dentistry. Ann Ist Super Sanita 51(3):229–235. https://doi.org/10.4415/ANN_15_03_11
45. Velasco MA, Narváez-Tovar CA, Garzón-Alvarado DA (2015) Design, materials, and mechanobiology of biodegradable scaffolds for bone tissue engineering. Biomed Res Int 2015:729076. https://doi.org/10.1155/2015/729076
46. Rodriguez A, Anastassov GE, Lee H et al (2003) Maxillary sinus augmentation with deproteinated bovine bone and platelet rich plasma with simultaneous insertion of endosseous implants. J Oral Maxillofac Surg 61(2):157–163. https://doi.org/10.1053/joms.2003.50041
47. Liu WJ, Li YY, Ding XT (2017) Cell adhesion pattern created by OSTE polymers. Biofabrication 9(2):025006. https://doi.org/10.1088/1758-5090/aa669c
48. Chen RX, Wan YQ, Wu WW et al (2019) A lotus effect-inspired flexible and breathable membrane with hierarchical electrospinning micro/nanofibers and ZnO nanowires. Mater Des 162:246–248. https://doi.org/10.1016/j.matdes.2018.11.041
49. Mitra T, Manna PJ, Raja STK et al (2015) Curcumin loaded nano graphene oxide reinforced fish scale collagen—a 3D scaffold biomaterial for wound healing applications. RSC Adv 5(119):98653–98665. https://doi.org/10.1039/c5ra15726a
50. Park JW, Kim YJ, Park CH et al (2009) Enhanced osteoblast response to an equal channel angular pressing-processed pure titanium substrate with microrough surface topography. Acta Biomater 5(8):3272–3280. https://doi.org/10.1016/j.actbio.2009.04.038
51. Lin KL, Xia LG, Gan JB et al (2013) Tailoring the nanostructured surfaces of hydroxyapatite bioceramics to promote protein adsorption, osteoblast growth, and osteogenic differentiation. ACS Appl Mater Interfaces 5(16):8008–8017. https://doi.org/10.1021/am402089w
52. Fu C, Bai HT, Zhu JQ et al (2017) Enhanced cell proliferation and osteogenic differentiation in electrospun PLGA/hydroxyapatite nanofibre scaffolds incorporated with graphene oxide. PLoS ONE 12(11):e0188352. https://doi.org/10.1371/journal.pone.0188352
53. Kim SH, Ha HJ, Ko YK et al (2007) Correlation of proliferation, morphology and biological responses of fibroblasts on LDPE with different surface wettability. J Biomater Sci Polym Ed 18(5):609–622. https://doi.org/10.1163/156856207780852514
54. Lee JH, Khang G, Lee JW et al (1998) Interaction of different types of cells on polymer surfaces with wettability gradient. J Colloid Interface Sci 205(2):323–330. https://doi.org/10.1006/jcis.1998.5688
55. Hughes FJ (2005) Color atlas of dental medicine: periodontology. Br Dent J 198(10):655–655. https://doi.org/10.1038/sj.bdj.4812424
56. Wang JL, Wang LN, Zhou ZY et al (2016) Biodegradable polymer membranes applied in guided bone/tissue regeneration: a review. Polymers 8(4):115. https://doi.org/10.3390/polym8040115
57. Einhorn TA, Gerstenfeld LC (2014) Fracture healing: mechanisms and interventions. Nat Rev Rheumatol 11(1):45–54. https://doi.org/10.1038/nrrheum.2014.164
58. Ho-Shui-Ling A, Bolander J, Rustom LE et al (2018) Bone regeneration strategies: engineered scaffolds, bioactive molecules and stem cells current stage and future perspectives. Biomaterials 180:143–162. https://doi.org/10.1016/j.biomaterials.2018.07.017
59. Rezwan K, Chen QZ, Blaker JJ et al (2006) Biodegradable and bioactive porous polymer/inorganic composite scaffolds for bone tissue engineering. Biomaterials 27(18):3413–3431. https://doi.org/10.1016/j.biomaterials.2006.01.039
60. Puppi D, Chiellini F, Piras AM et al (2010) Polymeric materials for bone and cartilage repair. Prog Polym Sci 35(4):403–440. https://doi.org/10.1016/j.progpolymsci.2010.01.006
61. Huang JH, Xia X, Zou Q et al (2019) The long-term behaviors and differences in bone reconstruction of three polymer-based scaffolds with different degradability. J Mater Chem B 7(48):7690–7703. https://doi.org/10.1039/c9tb02072a
62. Goor OJGM, Hendrikse SIS, Dankers PYW et al (2017) From supramolecular polymers to multi-component biomaterials. Chem Soc Rev 46(21):6621–6637. https://doi.org/10.1039/c7cs00564d
63. Jeevithan E, Zhao QB, Bin B et al (2013) Biomedical and pharmaceutical application of fish collagen and gelatin: a review. J

Nutr Ther 2(4):218–227. https://doi.org/10.6000/1929-5634.2013.02.04.6

64. Zhou T, Wang NP, Xue Y et al (2016) Electrospun tilapia collagen nanofibers accelerating wound healing via inducing keratinocytes proliferation and differentiation. Colloids Surf B Biointerfaces 143:415–422. https://doi.org/10.1016/j.colsurfb.2016.03.052
65. Hu LR, Xiang SJ, Liu JY et al (2022) Combigraft versus Bio-Oss/Bio-Gide in alveolar ridge preservation: a prospective randomized controlled trial. Oral Surg 15(2):163–169. https://doi.org/10.1111/ors.12687
66. Sumangali A, Naik AC, Mohan N et al (2021) Bone regenerative biomaterials in periapical surgery: a systemic review and meta-analysis. J Pharm BioAllied Sci 13(Suppl 2):S933–S937. https://doi.org/10.4103/jpbs.jpbs_386_21
67. Zhao SJ, Pinholt EM, Madsen JE et al (2000) Histological evaluation of different biodegradable and non-biodegradable membranes implanted subcutaneously in rats. J Cranio-Maxillofac Surg 28(2):116–122. https://doi.org/10.1054/jcms.2000.0127
68. Rothamel D, Schwarz F, Sager M et al (2005) Biodegradation of differently cross-linked collagen membranes: an experimental study in the rat. Clin Oral Implants Res 16(3):369–378. https://doi.org/10.1111/j.1600-0501.2005.01108.x